



Quantitative evaluation of structure-activity relationships in heterogeneous photocatalytic oxidation towards organic contaminants

Xiaonan Hu^a, Yang Ye^a, Wenbo Dong^b, Yichao Huang^c, Mingshan Zhu^{a,*}

^a Guangdong Key Laboratory of Environmental Pollution and Health, School of Environment, Jinan University, Guangzhou 511443, PR China

^b Shanghai Key Laboratory of Atmospheric Particle Pollution and Prevention, Department of Environmental Science & Engineering, Fudan University, Shanghai 200433, PR China

^c Department of Toxicology, School of Public Health; Key Laboratory of Environmental Toxicology of Anhui Higher Education Institutes, Anhui Medical University, Hefei 230032, PR China

ARTICLE INFO

Keywords:

Organic contaminants
Heterogeneous photocatalytic oxidation
Quantitative evaluation
Structure-activity relationships

ABSTRACT

Photocatalysis based advanced oxidation processes (AOPs) have drawn increasing attention for the removal of organic contaminants, while the relationships of the target organic contaminants with the intrinsic properties of the photocatalysts are usually neglected. Herein, the photocatalytic behaviors among ten kinds of organic contaminants and two heterojunction photocatalysts were comparatively investigated. Photocatalysts BiO-Cl_{0.75}I_{0.25}/g-C₃N₄ (BCI-CN) with abundant oxygen vacancies exhibited stronger absorption capacity towards light and quicker transfer efficiency of photoinduced carriers (factor $\eta_{1 \times 2}$) than BiOCl/g-C₃N₄ (BC-CN). Nevertheless, the redox ability (factor η_3) of BCI-CN was weaker than that of BC-CN. Factor $\eta_{1 \times 2}$ and η_3 synergistically and competitively affect the photocatalytic activities. Based on the differences and connections about intrinsic properties of BC(I)-CN photocatalysts, quantitative evaluation of structure-activity relationships among different organic contaminants and two photocatalysts were constructed, which provide valuable guidance for objectively evaluating the photocatalytic performance and precisely recognizing the compatibility among pollutants and photocatalysts.

1. Introduction

In order to efficiently eliminate recalcitrant organic contaminants in wastewater environment, the promising and eco-friendly semiconductor photocatalytic technologies have received considerable interests [1–4]. Various photocatalysts with different components, structures and properties have been constructed and developed to improve photocatalytic degradation performance [5–11]. The photocatalytic performance was usually estimated over one kind of photocatalyst and compared between/among several kinds of photocatalysts via selecting designated model contaminants [12–15]. However, if the model contaminant was changed to other types, the originally prominent photocatalytic performance over one kind of photocatalyst might become inferior, even none, and the order about the magnitude of the photocatalytic performance between/among several kinds of photocatalysts might be inverted. For example, Zhong et al. reported that perfluorooctanoic acid and trichloroacetic acid were more easily decomposed over BiOCl than on TiO₂. Nevertheless, benzoic acid and

acetic acid were more easily decomposed over TiO₂ than on BiOCl [16]. It was thus distinct that the photocatalytic performance of the photocatalysts was closely related to the as-selected organic contaminants.

It is well known that the photocatalytic performance depends on its intrinsic property of photocatalyst (including three factors: absorption efficiency towards light, separation and transfer efficiency of photo-generated carriers, and redox potential of photoinduced electrons and holes) [17–19]. When a photocatalyst is able to be motivated by light, sufficient redox potential is a prerequisite for stimulating pollutants to start to decompose, which is associated with the as-selected pollutants (“able” or “unable” question). When a pollutant is able to start to decompose, the above three factors play the synergistic and competitive roles in affecting the photocatalytic performance (“quick” or “slow” question) [20]. For instance, strong absorption ability toward light, quick transfer capacity of photoinduced carriers and large redox potential are beneficial to improve the photocatalytic performance (“synergistic role”). However, lower valence band and higher conduction band position (larger redox potential) indicate that the bandgap would

* Corresponding author.

E-mail address: zhumingshan@jnu.edu.cn (M. Zhu).

<https://doi.org/10.1016/j.apcatb.2022.121238>

Received 21 October 2021; Received in revised form 9 February 2022; Accepted 21 February 2022

Available online 22 February 2022

0926-3373/© 2022 Elsevier B.V. All rights reserved.

be wider and the photocatalysts might not generate more efficient and uncombined photoinduced holes and electrons under light illumination, thus will lead to the decrement of photocatalytic activities ("competitive role"). Therefore, the as-selected organic contaminants and the intrinsic properties of the photocatalysts together determine the photocatalytic degradation performance.

Normally, most researchers evaluate the photocatalytic performance via investigating the interaction between a specific organic pollutant and a designated photocatalyst [21,22]. However, different photocatalysts with different intrinsic properties give rise to different chemical interactions with different organic pollutants. The differences and connections on the decomposing behaviors induced by different photocatalysts towards various contaminants have been not systematically analyzed. It is significant to understand and exploit the selectivity and dependence among different contaminants and different photocatalysts.

Herein, two photocatalysts with different and comparable intrinsic properties were chosen to separately decompose various organic pollutants in water environment. Different possible photocatalytic mechanisms of the two photocatalysts were proposed and the structure-activity relationships among different contaminants and different photocatalysts were constructed via investigating the differences and connections on removal behaviors of ten contaminants and intrinsic properties of two photocatalysts. The order of difficulty level for the removal of these organic contaminants was accordingly obtained to quantitatively evaluate the structure-activity relationships among organic contaminants and photocatalysts.

2. Experimental section

2.1. Materials

All chemical reagents and organic pollutants were analytical grade without further treatment and purchased from Aladdin Chemical Reagent Company, except 5,5-dimethyl-1-pyrroline-*N*-oxide (DMPO) from Dojindo. The relevant information about as-investigated organic contaminants were listed in Table S1.

2.2. Synthesis of $\text{BiOCl}/\text{g-C}_3\text{N}_4$ (BC-CN) and $\text{BiOCl}_{0.75}\text{I}_{0.25}/\text{g-C}_3\text{N}_4$ (BCI-CN)

Photocatalysts $\text{BiOCl}/\text{g-C}_3\text{N}_4$ (denoted as BC-CN) and $\text{BiOCl}_{0.75}\text{I}_{0.25}/\text{g-C}_3\text{N}_4$ (denoted as BCI-CN) were synthesized via a facile coprecipitation method according to our previous reports [23]. In brief, $\text{g-C}_3\text{N}_4$ (denoted as CN) nanosheets were obtained by annealing melamine at 550 °C for 4 h with the ramping rate of 2.5 °C min⁻¹ in air and then via ultrasound in deionized (DI) water for 4 h. 5.82 g $\text{Bi}(\text{NO}_3)_3 \cdot 5\text{H}_2\text{O}$, 0.5 g polyvinylpyrrolidone (PVP, K-30) and 25 mL glycerol were successively added in the mixture of 0.3 g CN and 25 mL DI water at 80 °C. After fiercely stirring for 0.5 h, the KCl and KI aqueous solution of total 12 mM (0.67 g KCl + 0.50 g KI + 100 mL DI water) were dropwise introduced into the above suspension. The pH value was adjusted by $\text{NH}_3 \cdot \text{H}_2\text{O}$ to ca. 9.0. The mixed solution was reacted for another 1 h and then washed thoroughly for several times. The resulting precipitation was the BCI-CN. The BC-CN was synthesized in a similar way without adding KI. The amount of KCl was changed as 0.89 g to ensure the same molar mass for halogen atom.

2.3. Characterization

The morphologies and microstructures were observed via Field Emission Scanning Electron Microscope (FESEM, Nova NanoSem 450) and Field Emission Transmission Electron Microscope (FETEM, Tecnai G2 F20 S-Twin) combined with high resolution TEM (HRTEM). The phase structures were determined by X-ray powder diffraction (XRD, Rigaku Ultima IV) at a scanning speed of 10° min⁻¹. Fourier transform infrared (FTIR) spectra were obtained in a spectrometer (Shimadzu,

IRAffinity-1S). The texture information was measured by using the Brunauer-Emmett-Teller (BET) and Barrett-Joyner-Halenda (BJH) method on the Quantachrome instrument (Autosorb IQ2, USA). The UV-vis diffuse reflectance spectroscopy (UV-vis DRS) was performed on the JASCO V-770 with the integrating sphere mode. The Zeta potential was investigated on a zeta potential analyzer (Zetasizer Nano ZS90, Malvern). The steady-state photoluminescence (PL) spectra were conducted on the Edinburgh instruments (FLS1000). The transient photocurrent response and electrochemical impedance spectroscopy (EIS) data by using the L-type glassy carbon electrode were collected on the electrochemical workstation (CHI 760E). Electron spin resonance (ESR) spectra equipped with DMPO as the spin-trapping agent were detected on a Bruker spectrometer (A300, Germany). The valence band X-ray photoelectron spectroscopy (VB-XPS) were recorded on Thermo Scientific K-Alpha.

2.4. Photocatalytic performance assessment

The photocatalytic performance was evaluated in the photochemical reactor with a 500 W Xenon lamp and 290 nm cut-off filters as simulated solar light sources (XPA-VII, Nanjing xjiang electromechanical plant). 30 mg photocatalysts were dispersed in the cylindrical quartz tube including 50 mL, 10 mg·L⁻¹ organic pollutants. The temperature was retained at ca. 25 °C by circulating cooling water. After filtrating with 0.22 μm mixed cellulose membrane, the concentration of some organic pollutants was monitored by high performance liquid chromatography (HPLC, UltiMate 3000, Dionex). The mobile phase for bisphenol A (BPA) was a mixture of HPLC-grade methanol and ultrapure water (70/30, v/v) and the UV detector was operated at 280 nm. The mobile phase for carbamazepine (CBZ) was a mixture of HPLC-grade methanol and ultrapure water (80/20, v/v) and the UV detector was operated at 282 nm. The mobile phase for atenolol (ATL) was a mixture of HPLC-grade methanol and 0.01 M ammonium acetate aqueous solution (30/70, v/v) and the UV detector was operated at 224 nm. The concentration of other organic pollutants was determined by UV-vis spectrophotometer (Scinco, S-3100). The maximum absorbance for p-aminobenzoic acid (PABA), sulfamethoxazole (SMX), acetaminophen (APAP), p-hydroxybenzoic acid (PHBA), tetracycline (TC), ciprofloxacin (CIP) and p-hydroxyphenylacetic acid (HPAA) was at about 227 nm, 267 nm, 243 nm, 250 nm, 356 nm, 276 nm and 223 nm, respectively. The total organic carbon (TOC) and the mineralization degree was analyzed by Analytik Jena AG (Multi N/C UV HS/1, Germany).

3. Results and discussion

3.1. Photodegradation behaviors towards different organic contaminants

According to the results in Fig. S1, the adsorption, degradation and mineralization situations using BC-CN and BCI-CN photocatalysts towards various organic contaminants in water were summarized in Fig. 1 and Table S2. In details, the photocatalytic processes of each organic pollutant were displayed in Figs. S2-S11. As shown in Fig. 1a, after vigorously stirring in dark for 1 h to reach adsorption-desorption equilibrium, BC-CN displayed adsorption degree towards pollutants as follows: p-hydroxybenzoic acid (PHBA, 53.6%) > tetracycline (TC, 52.2%) > p-aminobenzoic acid (PABA, 49.6%) > p-hydroxyphenylacetic acid (HPAA, 43.7%) > ciprofloxacin (CIP, 43.1%) > bisphenol A (BPA, 0%) = sulfamethoxazole (SMX) = acetaminophen (APAP) = carbamazepine (CBZ) = atenolol (ATL). As for BCI-CN, the order of adsorption degree was PHBA (76.6%) > PABA (73.4%) > TC (67.5%) > CIP (59.8%) > HPAA (47.8%) > BPA (16.5%) > SMX (15.5%) > APAP (0%) = CBZ = ATL. Obviously, BCI-CN possessed stronger adsorption capacity towards the most organic pollutants than BC-CN, implying that BCI-CN was a good adsorbent material. Especially, pollutants containing -COOH group, such as PHBA, PABA, CIP and HPAA, was more easily adsorbed on the BCI-CN, which might be because electron withdrawing group

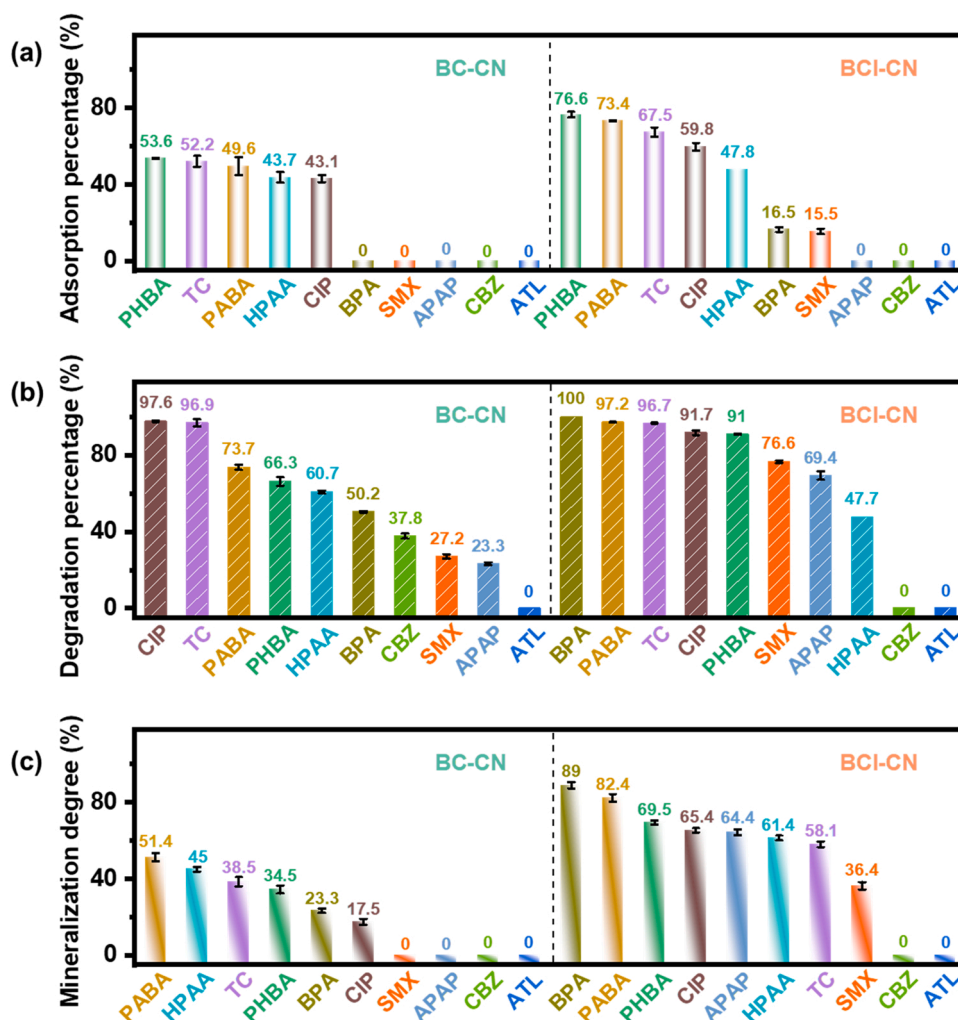


Fig. 1. The summary of adsorption situation in dark (a), degradation performance after simulated solar light irradiation of 60 min (b) and the corresponding mineralization degree (c) about various contaminants over BC-CN and BCI-CN. Reaction conditions: [Volume] = 50 mL, [Catalyst] = 0.6 g·L⁻¹ (30 mg), [Pollutant] = 10 mg·L⁻¹, [pH] = natural (7.5).

more preferred to be captured by surface oxygen vacancies with abundant localized electrons (which was confirmed later). Considering experimental errors, BC-CN and BCI-CN actually exhibited similar adsorption sequence for many pollutants.

However, the photocatalytic degradation performances on two photocatalysts were different (Fig. 1b). When BPA (100% for BCI-CN > 50.2% for BC-CN), PABA (97.2% > 73.7%), SMX (76.6% > 27.2%), APAP (69.4% > 23.3%) and PHBA (91.0% > 66.3%) was solely selected as the targeted contaminant, BCI-CN showed superior decomposition efficiencies than BC-CN under simulated solar irradiation of 1 h. As for CIP (91.7% < 97.6%), HPAA (47.7% < 60.7%) and CBZ (0% < 37.8%), BCI-CN showed inferior photocatalytic activities than BC-CN under identical conditions. Especially for HPAA and CBZ, BCI-CN had scarcely any activities in the photo-reaction step, whether or not pollutants could be adsorbed on the surface of the catalysts in dark. In addition, they both exhibited similar and outstanding degradation performance for TC (96.7% ≈ 96.9%) and could not bring any activities for ATL (0% = 0%).

In order to explore the oxidative species towards identical contaminant in different systems, SMX (or CBZ) was selected as the targeted object while the photocatalytic performance of BCI-CN (or BC-CN) was relatively better (Fig. S12). The isopropanol (IPA), Na₂C₂O₄ and CHCl₃ (k_{e-} , CHCl₃ = $3.0 \times 10^{10} \text{ M}^{-1} \text{ s}^{-1}$ and k_{HO^\bullet} , CHCl₃ = $5.0 \times 10^6 \text{ M}^{-1} \text{ s}^{-1}$) was the scavenger of HO[•], h⁺ and O₂^{•-} species, respectively [24,25]. As seen in these quenching experiments, HO[•] species both showed none

contribution on SMX and CBZ degradation, which was ascribed to the higher VB position of BC-CN and BCI-CN as evidenced by the following characterization. It was distinct that the contribution degree of active species for SMX removal on BCI-CN was O₂^{•-} > h⁺. As for CBZ decomposition, h⁺ and O₂^{•-} species respectively played the predominant and negligible roles on BC-CN. ESR spectra (Fig. S13) were also in accordance with above the results. No apparent signals of DMPO-HO[•] adducts in H₂O were detected whether in dark or under simulated solar light, implying that BCI-CN could not generate hydroxyl radicals. While in methanol solution, distinct characteristic ESR pattern of “1:1:1:1:1” indexed to DMPO-O₂^{•-} adducts was observed, demonstrating that O₂^{•-} could be generated over BCI-CN [26].

Fig. 1c depicted the corresponding mineralization results: PABA (51.4%) > HPAA (45%) > TC (38.5%) > PHBA (34.5%) > BPA (23.3%) > CIP (17.5%) > SMX (0%) = APAP = CBZ = ATL for BC-CN, and BPA (89%) > PABA (82.4%) > PHBA (69.5%) > CIP (65.4%) > APAP (64.4%) > HPAA (61.4%) > TC (58.1%) > SMX (36.4%) > CBZ (0%) = ATL for BCI-CN. It indicated that BCI-CN could more easily and efficiently transform pollutants into small molecules such as CO₂ and H₂O.

In brief summary, BCI-CN was a promising adsorber and mineralizer than BC-CN. However, BCI-CN sometimes showed relatively stronger or weaker photocatalytic degradation activity when compared with BC-CN (“Differences”). Besides, the degradation activities on BCI-CN and BC-CN sometimes were both none or approximately equal under certain

circumstance (“Similarities”). These differences and similarities suggested that photocatalytic performance strongly depended on the as-selected photocatalyst and as-investigated organic contaminant. Therefore, the investigations about structure-activity relationships among various organic contaminants and different BC(I)-CN photocatalysts were of great importance.

3.2. Architectural features of different photocatalysts

To uncover the underlying reasons which induced the formation of the differences and similarities on the photocatalytic performance, architectural features including the morphologies, phase structures and texture information of BC-CN and BCI-CN photocatalysts were firstly characterized. SEM and TEM images clearly depicted that they both had similar uniform thin sheet-like morphologies without obvious stacking (Fig. 2). HRTEM image of BCI-CN was displayed in Fig. S14. In addition to obvious layered structures, distinct lattice fringes with the spacing of 0.265 nm and 0.333 nm were also observed in BCI-CN, which were well matched with (110) plane of BCI and (002) plane of CN, respectively [27,28].

As can be seen in Fig. 3, XRD patterns of BC-CN and BCI-CN were similar to that of standard tetragonal BiOCl (JCPDS No. 06-0249) [29]. Compared with that of BC-CN, the diffraction peaks of BCI-CN exhibited slight blue shift in the enlarged XRD patterns, owing to the replacement of I⁻ with the larger radius (2.20 Å vs. 1.81 Å for Cl⁻) [30]. It revealed that bismuth oxyhalides in BCI-CN was definitely solid solution BiO-Cl_{0.75}I_{0.25} (abbreviated as BCI) rather than the physical compounds of BiOCl (BC) and BiOI. The formation of solid solution could improve the

intensity of internal electric field from the unique layer structures of BiOX (X = Cl, Br and I) which was composed of positive [Bi₂O₂] slabs sandwiched between negative double halogen atom slabs due to the enhancement of the polarization [31]. It was beneficial to efficient separation and quick transfer of photoinduced carriers.

Compared to pure BC and BCI (Fig. S15), BC-CN and BCI-CN both appeared a new diffraction peak at ca. 30 °C which indexed to (002) planes of CN. Besides, in contrast with pure CN, the shift of the new peak was ascribed to the strong interactions between CN and BC/BCI [32], indicating that the heterostructures in BC-CN and BCI-CN had been successfully constructed. In the FTIR spectra (Fig. S16), the typical peaks at 1650 cm⁻¹ - 1250 cm⁻¹ and 805 cm⁻¹ were assigned to the aromatic CN heterocycles (C=N, C-N stretching) and tri-s-triazine units in the g-C₃N₄ [33,34]. Besides, the sharp peak located at ca. 550 cm⁻¹ was attributed to the characteristic stretching vibration of Bi-O band [35]. These indicated the successful construction of the BC(I)-CN heterojunctions.

BCI-CN displayed higher BET specific surface area (72 m²/g) than BC-CN (45 m²/g) in Table S3, which accounted for its strong adsorption ability towards organic pollutants in wastewater [36]. The zeta potential of BCI-CN (30.8 mV) at initial pH = 7.5 was slightly higher than that of BC-CN (30.2 mV). Taking PABA, SMX and CBZ as typical examples, the acid dissociation constants (pK_{a1} and pK_{a2} value) of PABA, SMX and CBZ is respectively 2.4 and 4.8 [37], 1.6 and 5.7 [38], and 2.3 and 13.9 [39]. It means that PABA, SMX and CBZ was more negatively charged (compared to SMX), negatively charged and electrically neutral under experimental conditions, respectively. Combined with the above adsorption results, BCI-CN with more positive charge might be more

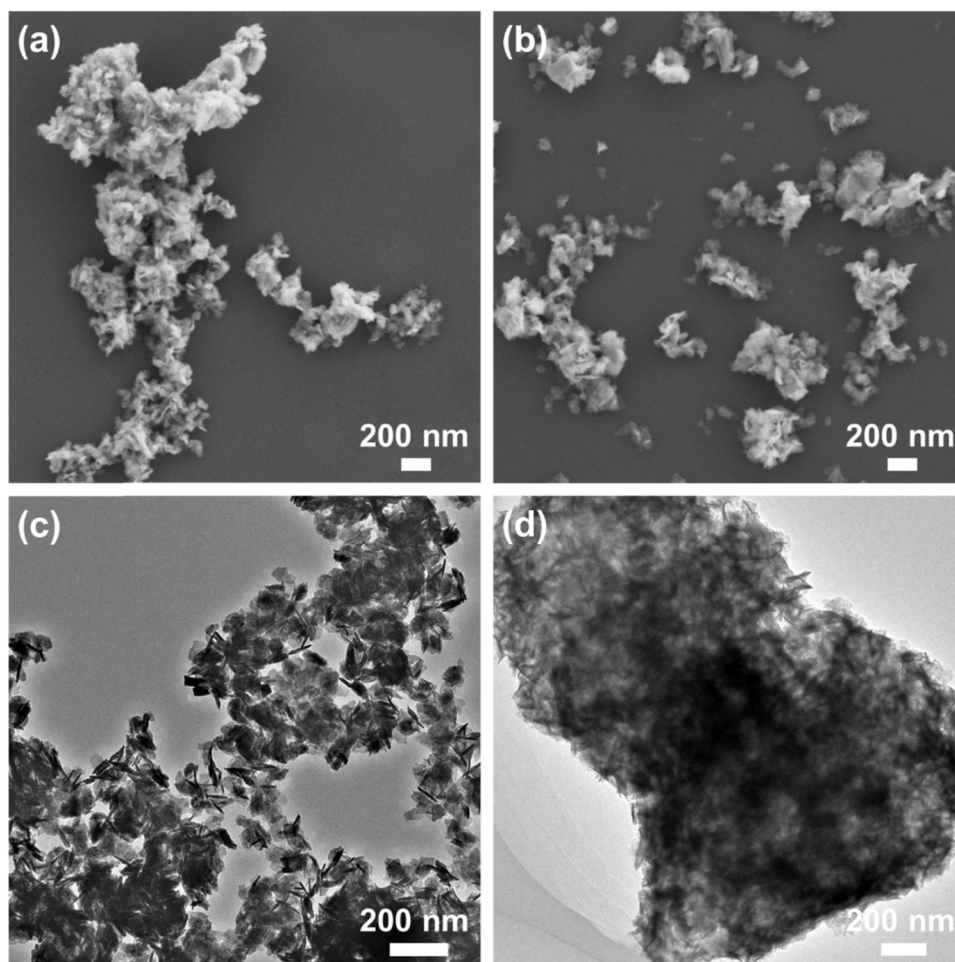


Fig. 2. SEM (a, b) and TEM (c, d) images of BC-CN (a, c) and BCI-CN (b, d).

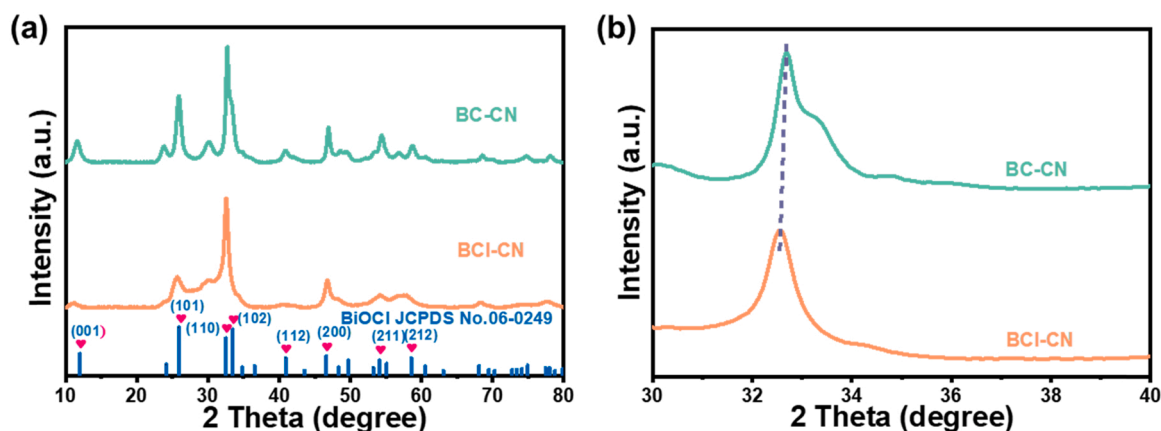


Fig. 3. XRD patterns of as-prepared samples (a) and the sectional corresponding enlarged XRD patterns (b).

conductive to adsorbing negatively charged pollutants via electrostatic interactions. Besides, surface rich oxygen vacancies in BCI-CN could serve as trap centers to reinforce the adsorption behaviors towards contaminants with opposite charge.

In order to thoroughly explore the structure-activity relationships, the intrinsic properties of the photocatalysts were worth discussing in details [40]. In principle, the absorption ability towards light (η_1), the recombination rate of photo-generated e^- and h^+ (η_2), and the redox capacity of carriers (η_3) are dominant factors which synergistically and competitively affect the photocatalytic efficiency (η) according to the equation ($\eta = \eta_1 \times \eta_2 \times \eta_3$) [41–43].

As depicted in Fig. 4a, the absorption edge of BCI-CN occurred a

prominent red-shifting compared with that of BC-CN. This revealed that BCI-CN possessed narrower band gap and stronger capture capacity towards light than BC-CN. Generally, the strong photoluminescence (PL) intensities imply the rapid recombination of photo-generated e^- and h^+ [44,45]. Fig. 4b indicated that BCI-CN could notably promote the transfer and suppress the recombination of photo-induced carriers. The transient photocurrent response and electrochemical impedance spectra under simulated solar irradiation were carried out to further unravel their charge transfer behaviors. It could be seen from Fig. 4c that the photocurrent density of BCI-CN was much higher than that of BC-CN. Meanwhile, BCI-CN obviously had a much smaller semicircular diameter in the Nyquist plot in comparison with BC-CN, suggesting that the

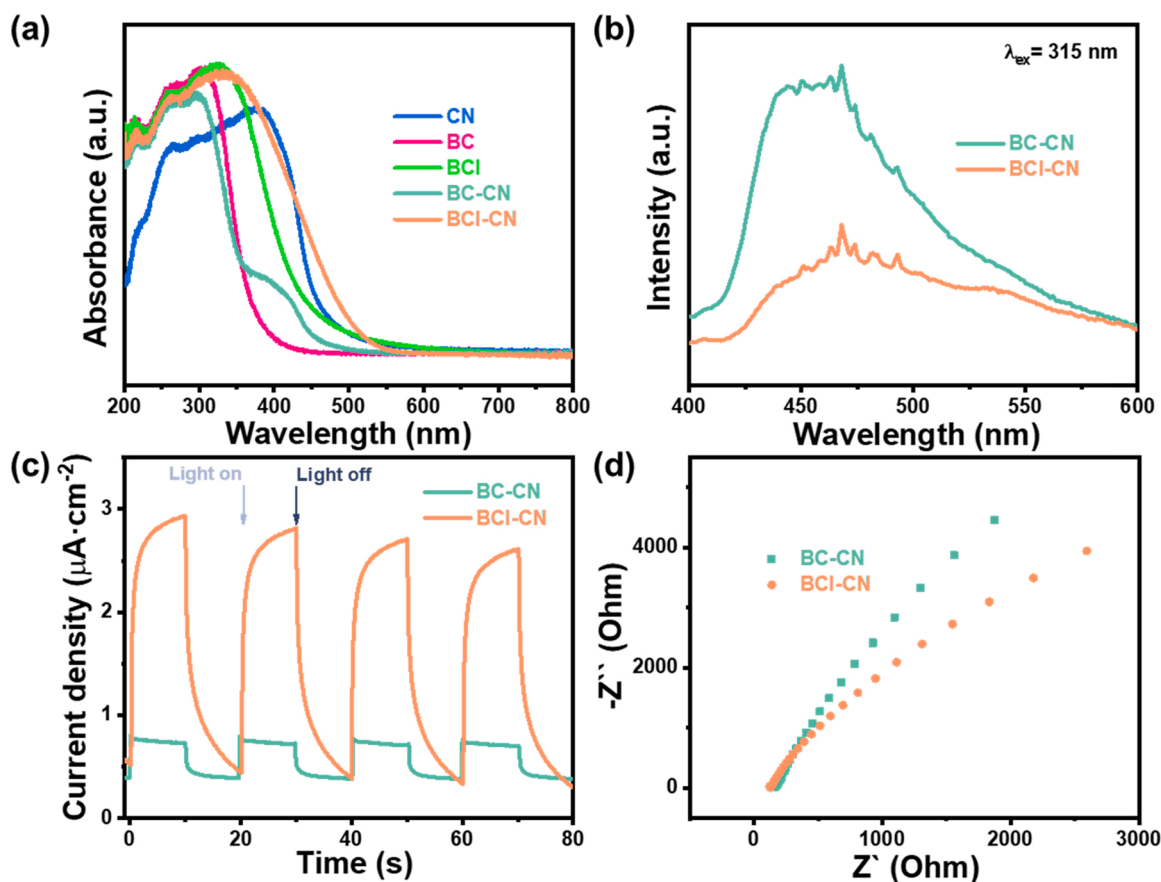


Fig. 4. UV-vis DRS spectra (a) and PL spectra (b) of as-prepared samples. The transient photocurrent response (c) and electrochemical impedance spectra (d) of BC-CN and BCI-CN under simulated solar irradiation.

impedance value of BCI-CN was much lower (Fig. 4d). These electrochemical results further shown that the lifetimes of photo-generated carriers were remarkably prolonged and the separation efficiencies of e^-h^+ pairs were efficiently enhanced in BCI-CN, which were well consistent with PL data.

Furthermore, BCI-CN possessed plentiful surface oxygen vacancies (OVs) than BC-CN, as evidenced by ESR. Distinctly in Fig. 5a, the signal intensity of BCI-CN at $g = 2.005$, which was the fingerprint evidence for the unpaired electrons trapped on oxygen vacancies [46], was much higher than that of BC-CN. It is generally recognized that the enhancement of surface oxygen vacancies which act as the electronic trapped center can be conducive to the efficient separation of photoinduced electrons and holes, thus remarkably boosting the photocatalytic activities [47]. Fig. S17 figured out that the photocatalytic activities toward BPA were notably declined when BCI-CN was calcined in different atmospheres. It was responsible that OVs were disappeared due to the supplement of oxygen gas under air atmosphere [48,49]. Under nitrogen or argon gas atmosphere, OVs are usually increased in the oxygen-poor environment [50,51]. However, OVs with abundant localized electrons could activate inert gas molecules to reduce Bi^{3+} ($Bi^{3+} + xe^- \rightarrow Bi^{(3-x)+}$) [52]. Thus, the concentration of OVs was also decreased. Accordingly, the appearance color of BCI-CN changed from yellow to dark or brown after calcination in N_2 or Ar. These results indirectly demonstrated that rich OVs were indeed existed on the BCI-CN and significant for good photocatalytic activities.

Therefore, BCI-CN with plentiful oxygen vacancies exhibited stronger absorption capacity towards light and better separation efficiency of

photoinduced carriers than BC-CN: (η_1 and η_2) of BCI-CN $>$ (η_1 and η_2) of BC-CN. These characters were responsible for the admirable photocatalytic removal activities on BCI-CN.

With respect to the comparison of redox properties (η_3), the band structures of these photocatalysts were then determined via the derived UV-vis DRS and VB-XPS. The corresponding band gap energies (E_g) deduced from the UV-vis DRS spectra could be analyzed by the plots of $(\alpha h\nu)^{1/2}$ versus $h\nu$ (the Tauc plot), where α , h and ν separately represented absorption coefficient, Planck constant and light frequency [53]. The band gap values of CN, BC and BCI solid solutions were estimated to be 2.53, 3.12 and 2.53 eV vs. NHE, respectively (Fig. S18). It should be noted that BC-CN showed two distinctive band gaps at about 2.57 and 3.00 eV which were characteristics of CN and BC, respectively. It implied that the heterojunctions in BC-CN might not be well established due to the absence of rich OVs. Comparatively, the heterojunctions in BCI-CN were nicely constructed, benefiting from surface plentiful OVs and suitable band structures. As depicted from the VB-XPS in Fig. S19, the valence band (VB) positions of CN, BC and BCI were approximately found to be at 1.49, 1.36 and 1.02 eV vs. NHE, respectively. The conduction band (CB) of CN, BC and BCI was respectively calculated to be -1.04 , -1.76 and -1.51 eV vs. NHE according to the energy band calculation formula ($E_{CB} = E_{VB} - E_g$) [54].

Based on above the results, the photocatalytic mechanisms of BC-CN and BCI-CN under simulated solar illumination were elaborately illustrated in Fig. 5b-c. Their transfer directions of photoinduced holes were similar: h^+ both transferred from the VB of CN to the VB of BC or BCI. Their VB positions were both lower than that of OH^-/HO^\bullet (+1.99 eV vs.

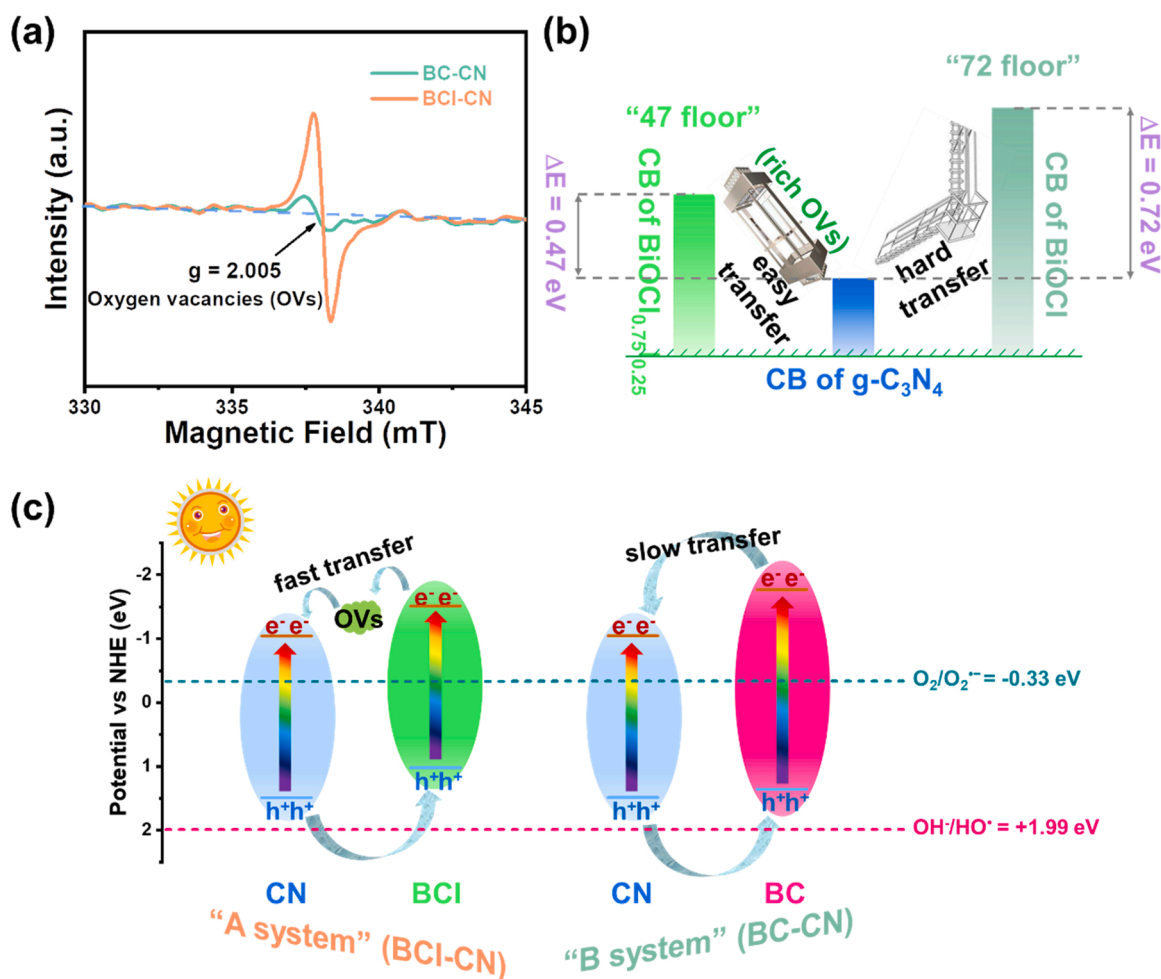


Fig. 5. ESR spectra of BC-CN and BCI-CN (a); The transfer manner of photoinduced e^- from the CB of BC(I) to the CB of $g-C_3N_4$ (b); Schematic illustration about energy band structures and separation situation of electron-hole pairs over BCI-CN and BC-CN catalysts (c).

NHE, pH = 7) [55], thus was thermodynamically unfavorable and could not convert OH^- into HO^\bullet by direct oxidization of h^+ , which matched with the results of aforesaid quenching experiments. The photo-generated holes on the VB became the major active species to continuously degrade organic contaminants.

However, their photogenerated electron flow directions were different. The e^- on the CB of BCI could rapidly migrate to the CB of CN with joint assistance of rich oxygen vacancies and nice heterojunctions for BCI-CN photocatalysts. As for BC-CN, owing to more negative CB value and the absence of plentiful OV, the e^- on the CB of BC hardly transferred to the CB of CN and preferred to stay on the CB of BC or triggered recombination with h^+ . The transfer difference for electrons could be explained and in analogy with the situations that how the people residing at high floor could choose to go downstairs to another building. The way of going downstairs involved using “elevators” (the presence of rich OV) and “stairs” (the absence of rich OV or said the presence of poor OV) between two “buildings” (CN and BC or BCI). The absolute difference value on the BC-CN between the CB of BC and the CB of CN was 0.72 eV, and the corresponding value on the BCI-CN was 0.47 eV. Accordingly, the BC of BC-CN and the BCI of BCI-CN were the people dwelling in the 72 floor and 47 floor, respectively. Profiting from the “elevators”, those people on the 47 floor for BCI-CN more tended to go downstairs to accomplish fast transfer. As for BC-CN with poor OV, the people on the higher 72 floor were unwilling to painfully go downstairs via “stairs” and preferred to stay at the same location. Meanwhile, these people on the 72 floor could be unable to “survive” for the long periods due to the lack of “movement”. These behaviors were well in accord with the fact that the faster recombination rates and the shorter lifetimes of photoinduced carries were detected on BC-CN. But their CB values were both relatively negative than that of $\text{O}_2/\text{O}_2^{\bullet-}$ (−0.33 eV vs. NHE, pH = 7), which gave rise to the formation of $\text{O}_2^{\bullet-}$ radicals via the reduction of dissolved O_2 with e^- [56,57], thus continuously decomposing organic pollutants into small molecules.

Therefore, the photoinduced electrons on BCI-CN system mainly focused on the CB of CN (−1.04 eV). As for on BC-CN system, the corresponding e^- centered at the CB of BC (−1.76 eV). Their photo-generated h^+ located on the VB of BC (+1.36 eV) for BC-CN and the VB of BCI (+1.02 eV) for BCI-CN, respectively. Apparently, the redox ability of BCI-CN was weaker than that of BC-CN (η_3 of BCI-CN < η_3 of BC-CN).

3.3. Construction of structure-activity relationships

In the light of all the aforementioned analyses, benefiting from the formation of solid solution, abundant OV and heterojunctions, BCI-CN could generate more efficient holes and electrons which were capable of surviving on the surface of photocatalysts as compared to BC-CN. BCI-CN was reasonably believed to be a promising photocatalytic material for degrading organic pollutants. But in some cases, the activities of BCI-CN were inferior to that of BC-CN. In fact, BC-CN possessed more powerful redox capacity than BCI-CN. It meant that suitable band structures and enough redox ability were also significant for high-efficient photocatalytic performance [58]. In other words, the η_1 , η_2 and η_3 factors played a synergy effect on the photocatalytic activities toward contaminants elimination. There were prominent advantages for BCI-CN in the first two factors (η_1 and η_2 : $\eta_1 \times \eta_2$ was collectively denoted as $\eta_{1 \times 2}$). BC-CN performed better in η_3 factor. In other words, $\eta_{1 \times 2}(\text{A}) > \eta_{1 \times 2}(\text{B})$, $\eta_3(\text{A}) < \eta_3(\text{B})$, in which A and B respectively represented the BCI-CN and BC-CN system.

According to the Eqs. (1–5), the ratio of photocatalytic activities for two photocatalysts toward identical organic pollutant ($\eta_{1 \times 2}(\%) \times \eta_3(\%)$) was approximately equal to k_3/k_2 , where $\eta_{1 \times 2}(\%) > 1$ and $\eta_3(\%) < 1$. It indicated that in comparison with numerical 1, the arithmetic product ($\eta_{1 \times 2}(\%) \times \eta_3(\%)$) represented that which factor had more contributions on the activities. Just like a “tug-of-war” competition, “quantity” (amounts of the generated unrecombined photoinduced carries) or “quality” (the corresponding single redox ability) was

regarded as the key to winning in the photocatalytic removal reaction (Fig. 6), which was tightly associated with as-selected target contaminant in water.

$$\eta(\text{A}) = \eta_{1 \times 2}(\text{A}) \times \eta_3(\text{A}) \quad (1)$$

$$\eta(\text{B}) = \eta_{1 \times 2}(\text{B}) \times \eta_3(\text{B}) \quad (2)$$

$$\frac{\eta(\text{A})}{\eta(\text{B})} = \frac{\eta_1 \times 2(\text{A}) \times \eta_3(\text{A})}{\eta_1 \times 2(\text{B}) \times \eta_3(\text{B})} = \eta_1 \times 2(\%) \times \eta_3(\%) \approx \frac{k_3}{k_2} \quad (3)$$

$$\eta_{1 \times 2}(\%) = \eta_{1 \times 2}(\text{A})/\eta_{1 \times 2}(\text{B}) \quad (4)$$

$$\eta_3(\%) = \eta_3(\text{A})/\eta_3(\text{B}) \quad (5)$$

where the k_3 and k_2 was the corresponding apparent reaction rate constant for A and B system, and was obtained by the pseudo first order kinetic equation based on Langmuir-Hinshelwood model ($-\ln(\text{C}/\text{C}_0) = kt$).

Fig. 7 depicted the pseudo first order kinetic fittings and the determined apparent rate constants towards two catalysts and various contaminants. Meanwhile, the corresponding structure-activity relationships among various organic contaminants and BC(I)-CN photocatalysts were summarized in Fig. 8.

When the k_3/k_2 value was greater than 1, the absorption ability towards light and the recombination rate of photo-generated e^- - h^+ were the major elements in determining the photocatalytic performance (Part I in Fig. 8). The effect of redox capacity was relatively minor and the redox potential required for inducing organic pollutant to degrade might be located between −1.04 eV and +1.02 eV based on the band structures. Besides, the bigger the k_3/k_2 value, the greater the influence of the $\eta_{1 \times 2}$ toward target pollutant. For example, the k_3/k_2 value for BPA was relatively maximal (20.5), thus suggesting that BPA might be most depended on the $\eta_{1 \times 2}$, the redox potential for BPA removal was lowest and BPA was most easily decomposed via photocatalysis among the as-investigated organic contaminants. PABA ($k_3/k_2 = 5.0$), SMX (4.4), APAP (4.2) and PHBA (3.2) were also mainly affected by the $\eta_{1 \times 2}$. It was worthy of note that the k_3 and k_2 value was all correspondingly approximately equal for SMX (0.022 min^{-1} and 0.005 min^{-1}), APAP (0.021 min^{-1} and 0.005 min^{-1}) and PHBA (0.019 min^{-1} and 0.006 min^{-1}), thus indicating that the coefficient of difficulty for these three kinds of pollutants removal was approximative. Here, $\text{O}_2^{\bullet-}$ and h^+ , especially $\text{O}_2^{\bullet-}$, could be major active species in the Part I.

When k_3/k_2 was close to 1, the effects of the $\eta_{1 \times 2}$ and η_3 were similar, such as for TC ($k_3/k_2 = 1.1$). If the k_3/k_2 value was between 0 and 1 (Part II), the function of the η_3 exceeded that of the $\eta_{1 \times 2}$, thereby hinting that the difficulty level for pollutant removal was moderate. For instance, the k_3/k_2 for CIP was only about 0.1, implying that enough powerful redox ability was relatively vital for CIP decomposition. If the k_3/k_2 value was zero ($k_3 = 0$ and $k_2 \neq 0$, Part III), the redox ability on BC-CN was still competent for contaminants removal, which was different from the situations on BCI-CN (“unable”). Here, holes played a predominant function in eliminating the hard organic pollutants (such as HPAA and CBZ) and the redox potential might be between +1.02 eV and +1.36 eV. When k_3 and k_2 was simultaneously zero (Part IV), the redox potential of BCI-CN and BC-CN could both be insufficient to induce pollutants degradation such as ATL. The redox potential of “at least greater than +1.36 eV or less than −1.04 eV” was demanded to degrade ATL. Conceivably, this type of pollutant was very hard to removal. Therefore, it can be concluded that the order of difficulty level for photocatalytic decomposition towards various organic contaminants in wastewater under the same operating conditions was $\text{BPA} < \text{PABA} < \text{SMX} \leq \text{APAP} \leq \text{PHBA} < \text{TC} < \text{CIP} < \text{HPAA} \approx \text{CBZ} < \text{ATL}$.

4. Conclusions

Although photocatalysis technology has been considered as an effective method to remove organic contaminants from water, the

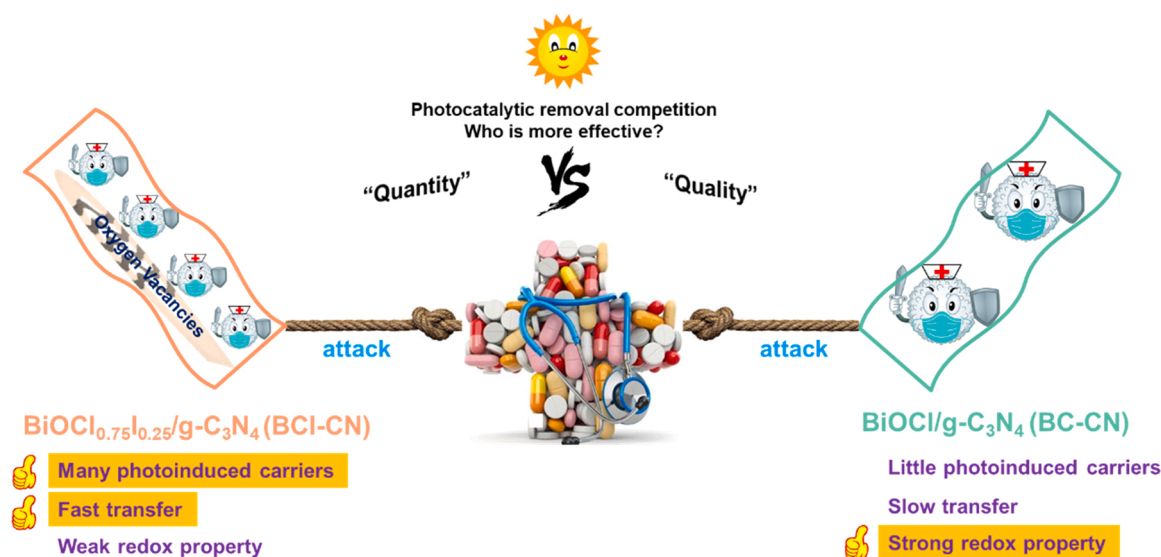


Fig. 6. The schematic diagram of a “tug-of-war” competition about eliminating organic pollutants in water via photocatalysis.

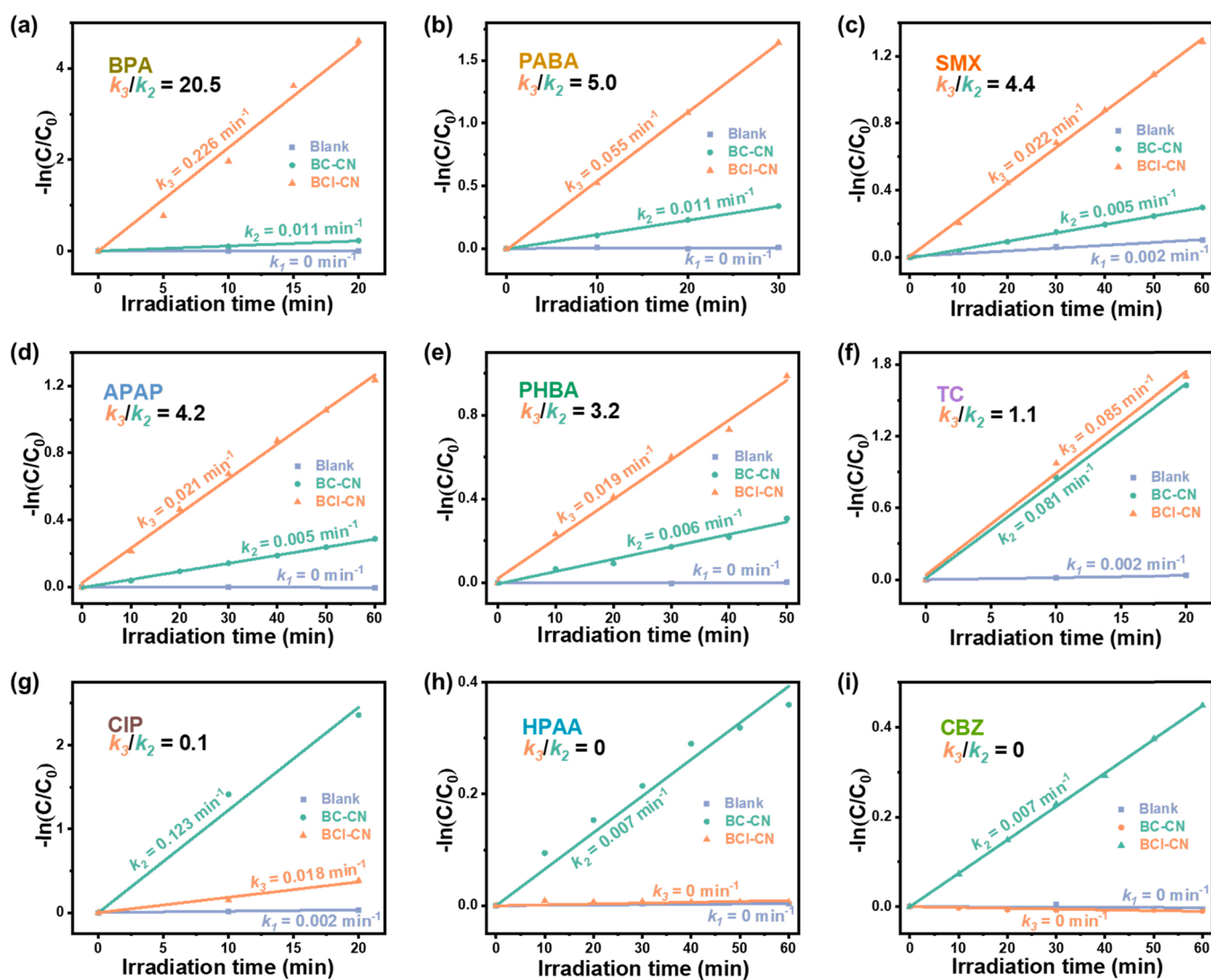


Fig. 7. The apparent reaction rate constants in the photocatalytic processes toward different organic contaminants (a, BPA; b, PABA; c, SMX; d, APAP; e, PHBA; f, TC; g, CIP; h, HPAA; i, CBZ) over BC-CN and BCI-CN catalysts. The k_1 , k_2 and k_3 represented the apparent reaction rate constants in blank (without any photocatalysts), on BC-CN and BCI-CN, respectively.

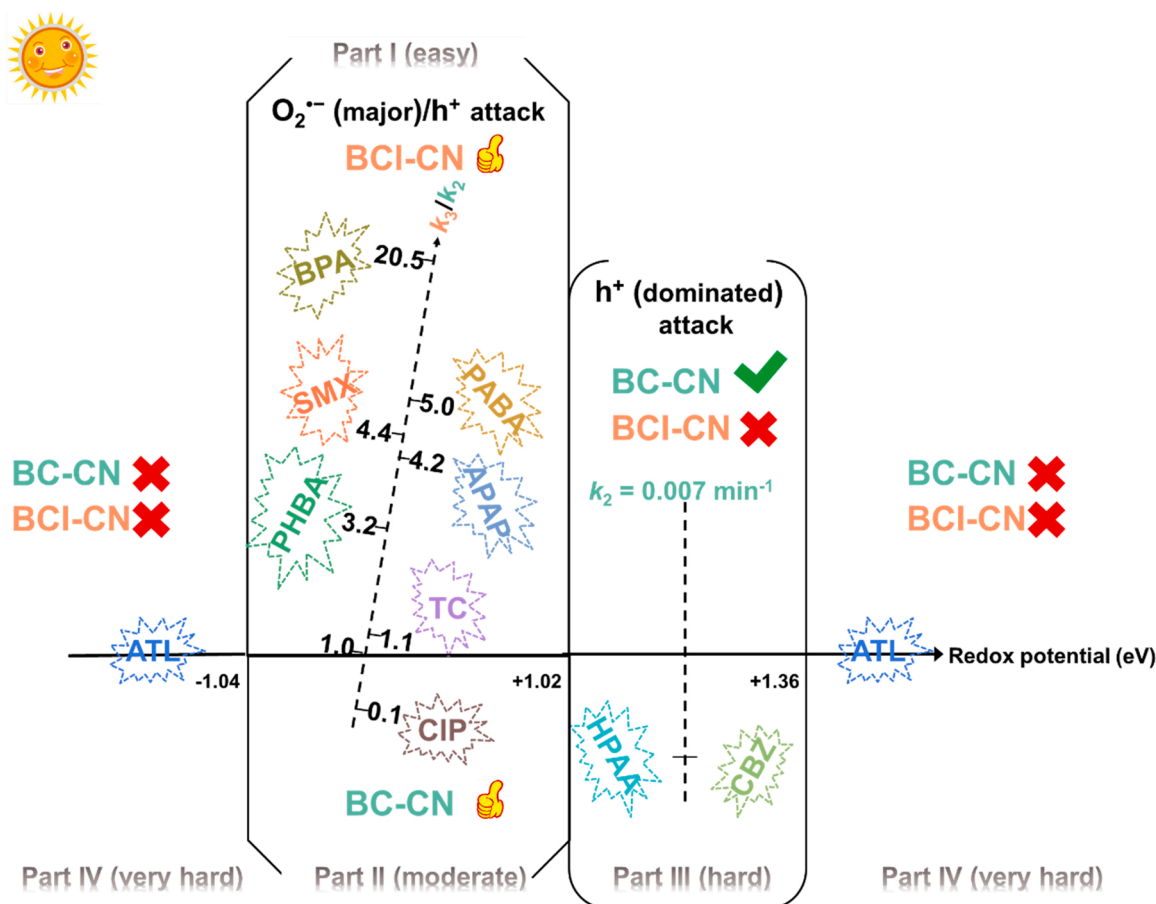


Fig. 8. The structure-activity relationships among different photocatalysts and various organic contaminants.

relationships of the as-selected target organic contaminants with the intrinsic properties of the photocatalysts are always blanked. In this study, we comparatively evaluated the photocatalytic behaviors among ten kinds of organic contaminants and two heterojunction photocatalysts (BC-CN and BCI-CN with rich oxygen vacancies) under simulated solar irradiation. By comparing the photocatalytic efficiency (η) depended on the intrinsic properties of the photocatalysts according to the equation ($\eta = \eta_1 \times \eta_2 \times \eta_3$, where η_1 is absorption ability towards light, η_2 is the recombination rate of photo-generated e^- and h^+ , and η_3 is the redox capacity of carriers) and the ratio of photocatalytic activities for two photocatalysts toward identical organic pollutant ($k_{\text{BCI-CN}}/k_{\text{BC-CN}} \approx \eta_{1 \times 2}(\%) \times \eta_3(\%)$, where $\eta_{1 \times 2}(\%) > 1$ and $\eta_3(\%) < 1$), the quantitative evaluation on the structure-activity relationships among different organic contaminants and two photocatalysts was constructed. The order of decomposition difficulty level under the same operating conditions was $\text{BPA} < \text{PABA} < \text{SMX} \leq \text{APAP} \leq \text{PHBA} < \text{TC} < \text{CIP} < \text{HPAA} \approx \text{CBZ} < \text{ATL}$.

The findings in the present work tell us that the value of one photocatalyst can be not simply evaluated via the degradation performance of one pollutant. Rational match and precise removal among photocatalysts and contaminants are significant. In the potential environmental applications, based on the differences and connections in intrinsic properties of photocatalysts, how to choose appropriate catalyst and correlate with specific pollutant is meaningful for the evaluation and the enhancement of decomposition performance, and the interactions and the compatibilities among different catalysts and various pollutants are deserved to be further focused in the wastewater treatment processes. In the future, not only the inherent properties of photocatalysts, but also the structure attributes (including acid dissociation constants and functional groups) of pollutants should be more forcefully

correlated together.

CRediT authorship contribution statement

Xiaonan Hu: Conceptualization, Data curation, Formal analysis, Methodology, Validation, Writing – original draft. **Yang Ye:** Data curation, Formal analysis, Methodology. **Wenbo Dong:** Conceptualization, Writing – review & editing. **Yichao Huang:** Formal analysis, Writing – review & editing. **Mingshan Zhu:** Conceptualization, Funding acquisition, Supervision, Writing – review & editing.

Declaration of Competing Interest

The authors declare that they have no known competing financial interests or personal relationships that could have appeared to influence the work reported in this paper.

Acknowledgements

This work was supported by Guangdong Basic and Applied Basic Research Foundation (Nos. 2020B1515020038 and 2021A1515110914) and the Pearl River Talent Recruitment Program of Guangdong Province (2019QN01L148).

Appendix A. Supporting information

Supplementary data associated with this article can be found in the online version at [doi:10.1016/j.apcatb.2022.121238](https://doi.org/10.1016/j.apcatb.2022.121238).

References

- [1] A.F. Marye, T.D. Maria, Heterogeneous photocatalysis, *Chem. Rev.* 93 (1993) 341–357.
- [2] B.C. Hodges, E.L. Cates, J.H. Kim, Challenges and prospects of advanced oxidation water treatment processes using catalytic nanomaterials, *Nat. Nanotechnol.* 13 (2018) 642–650.
- [3] Z. Xie, Y.P. Peng, L. Yu, C. Xing, M. Qiu, J. Hu, H. Zhang, Solar-inspired water purification based on emerging 2D materials: status and challenges, *Sol. RRL* 4 (2020) 1900400.
- [4] C.G. Lee, H. Javed, D. Zhang, J.H. Kim, P. Westerhoff, Q. Li, P.J.J. Alvarez, Porous electrospun fibers embedding TiO_2 for adsorption and photocatalytic degradation of water pollutants, *Environ. Sci. Technol.* 52 (2018) 4285–4293.
- [5] X. Li, J.G. Yu, M. Jaroniec, Hierarchical photocatalysts, *Chem. Soc. Rev.* 45 (2016) 2603–2636.
- [6] J. Low, J. Yu, M. Jaroniec, S. Wageh, A.A. Al-Ghamdi, Heterojunction photocatalysts, *Adv. Mater.* 29 (2017) 1601694.
- [7] H. Wang, L. Zhang, Z. Chen, J. Hu, S. Li, Z. Wang, J. Liu, X. Wang, Semiconductor heterojunction photocatalysts: design, construction, and photocatalytic performances, *Chem. Soc. Rev.* 43 (2014) 5234–5244.
- [8] Q. Zheng, D.P. Durkin, J.E. Elenewski, Y. Sun, N.A. Banek, L. Hua, H. Chen, M. J. Wagner, W. Zhang, D. Shuai, Visible-light-responsive graphitic carbon nitride: rational design and photocatalytic applications for water treatment, *Environ. Sci. Technol.* 50 (2016) 12938–12948.
- [9] M.J. Arlos, M.M. Hatat-Fraile, R. Liang, L.M. Bragg, N.Y. Zhou, S.A. Andrews, M. R. Servos, Photocatalytic decomposition of organic pollutants using immobilized TiO_2 having different isoelectric points, *Water Res.* 101 (2016) 351–361.
- [10] D. Zhang, C. Lee, H. Javed, P. Yu, J.H. Kim, P.J.J. Alvarez, Easily recoverable, micrometer-sized TiO_2 hierarchical spheres decorated with cyclodextrin for enhanced photocatalytic degradation of organic pollutants, *Environ. Sci. Technol.* 52 (2018) 12402–12411.
- [11] C. Liu, X. Ren, F. Lin, X. Fu, X. Lin, T. Li, K. Sun, J. Huang, Structure of the $\text{Au}_{23-x}\text{Ag}_x(\text{S-Adm})_{15}$ nanocluster and its application for photocatalytic degradation of organic pollutants, *Angew. Chem. Int. Ed.* 58 (2019) 11335–11339.
- [12] S. Ding, J. Niu, Y. Bao, L. Hu, Evidence of superoxide radical contribution to demineralization of sulfamethoxazole by visible-light-driven $\text{Bi}_2\text{O}_3/\text{Bi}_2\text{O}_2\text{CO}_3/\text{Sr}_6\text{Bi}_2\text{O}_9$ photocatalyst, *J. Hazard. Mater.* 262 (2013) 812–818.
- [13] T.B. Nguyen, C.P. Huang, R.-a. Doong, C.W. Chen, C.D. Dong, Visible-light photodegradation of sulfamethoxazole (SMX) over Ag-P-codoped g- C_3N_4 (Ag-P@UCN) photocatalyst in water, *Chem. Eng. J.* 384 (2020), 123383.
- [14] C. Zhao, Z. Liao, W. Liu, F. Liu, J. Ye, J. Liang, Y. Li, Carbon quantum dots modified tubular g- C_3N_4 with enhanced photocatalytic activity for carbamazepine elimination: mechanisms, degradation pathway and DFT calculation, *J. Hazard. Mater.* 381 (2020), 120957.
- [15] L. Tang, J.-j Wang, C.-t Jia, G.-x Lv, G. Xu, W.-t Li, L. Wang, J.-y Zhang, M.-h Wu, Simulated solar driven catalytic degradation of psychiatric drug carbamazepine with binary BiVO_4 heterostructures sensitized by graphene quantum dots, *Appl. Catal. B Environ.* 205 (2017) 587–596.
- [16] J. Zhong, Y. Zhao, L. Ding, H. Ji, W. Ma, C. Chen, J. Zhao, Opposite photocatalytic oxidation behaviors of BiOCl and TiO_2 : direct hole transfer vs. indirect-OH oxidation, *Appl. Catal. B Environ.* 241 (2019) 514–520.
- [17] S. Zhu, D. Wang, Photocatalysis: basic principles, diverse forms of implementations and emerging scientific opportunities, *Adv. Energy Mater.* 7 (2017) 1700841.
- [18] M.N. Chong, B. Jin, C.W. Chow, C. Saint, Recent developments in photocatalytic water treatment technology: a review, *Water Res.* 44 (2010) 2997–3027.
- [19] W. Liu, Y. Li, F. Liu, W. Jiang, D. Zhang, J. Liang, Visible-light-driven photocatalytic degradation of diclofenac by carbon quantum dots modified porous g- C_3N_4 : mechanisms, degradation pathway and DFT calculation, *Water Res.* 151 (2019) 8–19.
- [20] S.K. Loeb, P.J.J. Alvarez, J.A. Brame, E.L. Cates, W. Choi, J. Crittenden, D. D. Dionysiou, Q. Li, G. Li-Puma, X. Quan, D.L. Sedlak, T.D. Waite, P. Westerhoff, J. H. Kim, The technology horizon for photocatalytic water treatment: sunrise or sunset? *Environ. Sci. Technol.* 53 (2019) 2937–2947.
- [21] X. Chen, C. Yu, R. Zhu, N. Li, J. Chen, Q. Lin, S. Xu, X. Chen, H. Wang, Photocatalytic performance and mechanism of Z-Scheme $\text{CuBi}_2\text{O}_4/\text{Ag}_3\text{PO}_4$ in the degradation of diclofenac sodium under visible light irradiation: effects of pH, H_2O_2 , and $\text{S}_2\text{O}_8^{2-}$, *Sci. Total Environ.* 711 (2020), 134643.
- [22] J. Zhang, W. Zhao, Z. Li, G. Lu, M. Zhu, Visible-light-assisted peroxymonosulfate activation over Fe(II)/V(IV) self-doped FeVO_4 nanobelts with enhanced sulfamethoxazole degradation: performance and mechanism, *Chem. Eng. J.* 403 (2021), 126384.
- [23] X. Hu, Y. Zhang, B. Wang, H. Li, W. Dong, Novel g- $\text{C}_3\text{N}_4/\text{BiOCl}_{1-x}$ nanosheets with rich oxygen vacancies for enhanced photocatalytic degradation of organic contaminants under visible and simulated solar light, *Appl. Catal. B Environ.* 256 (2019), 117789.
- [24] G.V. Buxton, C. Greenstock, W.P. Hellman, A.B. Ross, Critical review of rate constants for reactions of hydrated electrons, hydrogen atoms and hydroxyl radicals ($^{\bullet}\text{OH}/^{\bullet}\text{O}$) in aqueous solution, *J. Phys. Chem. Ref. Data* 17 (1988) 513–886.
- [25] S. Hwang, S.G. Huling, S. Ko, Fenton-like degradation of MTBE: effects of iron counter anion and radical scavengers, *Chemosphere* 78 (2010) 563–568.
- [26] X. Chen, H. Yang, C. Au, S. Tian, Y. Xiong, Y. Chang, Efficiency and mechanism of pollutant degradation and bromate inhibition by faceted CeO_2 catalyzed ozonation: experimental and theoretical study, *Chem. Eng. J.* 390 (2020), 124480.
- [27] R. Fu, X. Zeng, L. Ma, S. Gao, Q. Wang, Z. Wang, B. Huang, Y. Dai, J. Lu, Enhanced photocatalytic and photoelectrochemical activities of reduced $\text{TiO}_{2-x}/\text{BiOCl}$ heterojunctions, *J. Power Sources* 312 (2016) 12–22.
- [28] L. Wang, G. Zhou, Y. Tian, L. Yan, M. Deng, B. Yang, Z. Kang, H. Sun, Hydroxyl decorated g- C_3N_4 nanoparticles with narrowed bandgap for high efficient photocatalyst design, *Appl. Catal. B Environ.* 244 (2019) 262–271.
- [29] P. Zhou, Y. Shen, S. Zhao, G. Li, B. Cui, D. Wei, Y. Shen, Synthesis of clinoptilolite-supported $\text{BiOCl}/\text{TiO}_2$ heterojunction nanocomposites with highly-enhanced photocatalytic activity for the complete degradation of xanthates under visible light, *Chem. Eng. J.* 407 (2021), 126697.
- [30] K. Kaup, A. Assoud, J. Liu, L.F. Nazar, Fast Li-ion conductivity in superadamantanoid lithium thioborate halides, *Angew. Chem. Int. Ed.* 133 (2021) 7051–7056.
- [31] X. Ren, J. Li, X. Cao, B. Wang, Y. Zhang, Y. Wei, Synergistic effect of internal electric field and oxygen vacancy on the photocatalytic activity of BiOBr_{1-x} with isomorphous fluorine substitution, *J. Colloid Interface Sci.* 554 (2019) 500–511.
- [32] M. Wu, X. He, B. Jing, T. Wang, C. Wang, Y. Qin, Z. Ao, S. Wang, T. An, Novel carbon and defects co-modified g- C_3N_4 for highly efficient photocatalytic degradation of bisphenol A under visible light, *J. Hazard. Mater.* 384 (2020), 121323.
- [33] H. Yang, W. Wang, X. Wu, M.S. Siddique, Z. Su, M. Liu, W. Yu, Reducing ROS generation and accelerating the photocatalytic degradation rate of PPCPs at neutral pH by doping Fe-N-C to g- C_3N_4 , *Appl. Catal. B Environ.* 301 (2022), 120790.
- [34] M. Wang, P. Guo, Y. Zhang, C. Lv, T. Liu, T. Chai, Y. Xie, Y. Wang, T. Zhu, Synthesis of hollow lantern-like Eu(III)-doped g- C_3N_4 with enhanced visible light photocatalytic performance for organic degradation, *J. Hazard. Mater.* 349 (2018) 224–233.
- [35] M. Zhang, C. Lai, B. Li, D. Huang, G. Zeng, P. Xu, L. Qin, S. Liu, X. Liu, H. Yi, M. Li, C. Chu, Z. Chen, Rational design 2D/2D $\text{BiOBr}/\text{CDs}/\text{g-C}_3\text{N}_4$ Z-scheme heterojunction photocatalyst with carbon dots as solid-state electron mediators for enhanced visible and NIR photocatalytic activity: kinetics, intermediates, and mechanism insight, *J. Catal.* 369 (2019) 469–481.
- [36] Y. Zhang, W. Cui, W. An, L. Liu, Y. Liang, Y. Zhu, Combination of photoelectrocatalysis and adsorption for removal of bisphenol A over TiO_2 -graphene hydrogel with 3D network structure, *Appl. Catal. B Environ.* 221 (2018) 36–46.
- [37] L. Zhou, Y. Ji, C. Zeng, Y. Zhang, Z. Wang, X. Yang, Aquatic photodegradation of sunscreen agent p-aminobenzoic acid in the presence of dissolved organic matter, *Water Res.* 47 (2013) 153–162.
- [38] S. Naraginti, Y.-Y. Yu, Z. Fang, Y.-C. Yong, Novel tetrahedral $\text{Ag}_3\text{PO}_4/\text{N-RGO}$ for photocatalytic detoxification of sulfamethoxazole: process optimization, transformation pathways and biotoxicity assessment, *Chem. Eng. J.* 375 (2019), 122035.
- [39] H. Zhou, L. Lai, Y. Wan, Y. He, G. Yao, B. Lai, Molybdenum disulfide (MoS_2): a versatile activator of both peroxymonosulfate and persulfate for the degradation of carbamazepine, *Chem. Eng. J.* 384 (2020), 123264.
- [40] R. Chen, S. Pang, H. An, J. Zhu, S. Ye, Y. Gao, F. Fan, C. Li, Charge separation via asymmetric illumination in photocatalytic Cu_2O particles, *Nat. Energy* 3 (2018) 655–663.
- [41] J. Ran, M. Jaroniec, S.Z. Qiao, Cocatalysts in semiconductor-based photocatalytic CO_2 reduction: achievements, challenges, and opportunities, *Adv. Mater.* 30 (2018) 1704649.
- [42] J. Byun, K.A.I. Zhang, Designing conjugated porous polymers for visible light-driven photocatalytic chemical transformations, *Mater. Horiz.* 7 (2020) 15–31.
- [43] Z. Wang, L. Wang, Progress in designing effective photoelectrodes for solar water splitting, *Chin. J. Catal.* 39 (2018) 369–378.
- [44] B. Niu, Z. Xu, A stable $\text{Ta}_3\text{N}_5/\text{PANI}$ core-shell photocatalyst: shell thickness effect, high-efficient photocatalytic performance and enhanced mechanism, *J. Catal.* 371 (2019) 175–184.
- [45] Y. Guo, W. Shi, Y. Zhu, Y. Xu, F. Cui, Enhanced photoactivity and oxidizing ability simultaneously via internal electric field and valence band position by crystal structure of bismuth oxyiodide, *Appl. Catal. B Environ.* 262 (2020), 118262.
- [46] Y. Mao, P. Wang, L. Li, Z. Chen, H. Wang, Y. Li, S. Zhan, Unravelling the synergy between oxygen vacancies and oxygen substitution in BiO_{2-x} for efficient molecular-oxygen activation, *Angew. Chem. Int. Ed.* 59 (2020) 3685–3690.
- [47] S.Q. Guo, X.H. Zhu, H.J. Zhang, B.C. Gu, W. Chen, L. Liu, P.J.J. Alvarez, Improving photocatalytic water treatment through nanocrystal engineering: mesoporous nanosheet-assembled 3D BiOCl hierarchical nanostructures that induce unprecedented large vacancies, *Environ. Sci. Technol.* 52 (2018) 6872–6880.
- [48] H. Li, F. Qin, Z. Yang, X. Cui, J. Wang, L. Zhang, New reaction pathway induced by plasmon for selective benzyl alcohol oxidation on BiOCl possessing oxygen vacancies, *J. Am. Chem. Soc.* 139 (2017) 3513–3521.
- [49] J. Tian, Z. Chen, X. Deng, Q. Sun, Z. Sun, W. Li, Improving visible light driving degradation of norfloxacin over core-shell hierarchical BiOCl microspherical photocatalyst by synergistic effect of oxygen vacancy and nanostructure, *Appl. Surf. Sci.* 453 (2018) 373–382.
- [50] H. Li, J. Shang, Z. Ai, L. Zhang, Efficient visible light nitrogen fixation with BiOBr nanosheets of oxygen vacancies on the exposed {001} facets, *J. Am. Chem. Soc.* 137 (2015) 6393–6399.
- [51] X. Pan, M.Q. Yang, X. Fu, N. Zhang, Y.J. Xu, Defective TiO_2 with oxygen vacancies: synthesis, properties and photocatalytic applications, *Nanoscale* 5 (2013) 3601–3614.
- [52] Y. Huang, H. Li, M.S. Balogun, W. Liu, Y. Tong, X. Lu, H. Ji, Oxygen vacancy induced bismuth oxyiodide with remarkably increased visible-light absorption and superior photocatalytic performance, *ACS Appl. Mater. Interfaces* 6 (2014) 22920–22927.

- [53] P. Li, Z. Zhou, Q. Wang, M. Guo, S. Chen, J. Low, R. Long, W. Liu, P. Ding, Y. Wu, Y. Xiong, Visible-light-driven nitrogen fixation catalyzed by $\text{Bi}_5\text{O}_7\text{Br}$ nanostructures: enhanced performance by oxygen vacancies, *J. Am. Chem. Soc.* 142 (2020) 12430–12439.
- [54] J. Song, J. Dai, P. Zhang, Y. Liu, J. Yu, B. Ding, $\text{g-C}_3\text{N}_4$ encapsulated ZrO_2 nanofibrous membrane decorated with CdS quantum dots: a hierarchically structured, self-supported electrocatalyst toward synergistic NH_3 synthesis, *Nano Res.* 14 (2020) 1479–1487.
- [55] S. Zhang, L. Wang, C. Liu, J. Luo, J. Crittenden, X. Liu, T. Cai, J. Yuan, Y. Pei, Y. Liu, Photocatalytic wastewater purification with simultaneous hydrogen production using MoS_2 QD-decorated hierarchical assembly of ZnIn_2S_4 on reduced graphene oxide photocatalyst, *Water Res.* 121 (2017) 11–19.
- [56] Y. Fan, W. Ma, D. Han, S. Gan, X. Dong, L. Niu, Convenient recycling of 3D $\text{AgX}/\text{graphene}$ aerogels ($\text{X} = \text{Br}, \text{Cl}$) for efficient photocatalytic degradation of water pollutants, *Adv. Mater.* 27 (2015) 3767–3773.
- [57] J. Xiong, X. Li, J. Huang, X. Gao, Z. Chen, J. Liu, H. Li, B. Kang, W. Yao, Y. Zhu, CN/rGO@BPQDs high-low junctions with stretching spatial charge separation ability for photocatalytic degradation and H_2O_2 production, *Appl. Catal. B Environ.* 266 (2020), 118602.
- [58] W. Wang, G. Li, T. An, D.K.L. Chan, J.C. Yu, P.K. Wong, Photocatalytic hydrogen evolution and bacterial inactivation utilizing sonochemical-synthesized $\text{g-C}_3\text{N}_4/\text{red phosphorus}$ hybrid nanosheets as a wide-spectral-responsive photocatalyst: the role of type I band alignment, *Appl. Catal. B Environ.* 238 (2018) 126–135.